ECCOMAS Congress 2016
VII European Congress on Computational Methods in Applied Sciences and Engineering
M. Papadrakakis, V. Papadopoulos, G. Stefanou, V. Plevris (eds.)
Crete Island, Greece, 5–10 June 2016

MULTI-FIDELITY EXTENSION TO NON-INTRUSIVE PROPER ORTHOGONAL DECOMPOSITION BASED SURROGATES

Benamara T.[*,1,2,3], **Breitkopf P.**[1], **Lepot I.**[2], **and Sainvitu C.**[2]

[1]Laboratoire Roberval UMR 7337 UTC-CNRS
Université de Technologie de Compiègne, 60200 Compiègne, France
e-mail: {tariq.benamara, piotr.breitkopf}@utc.fr

[2] Cenaero ASBL
Rue des Frères Wright 29, 6041 Gosselies, Belgium
e-mail: {caroline.sainvitu, ingrid.lepot}@cenaero.be

[3] Snecma Villaroche
Rond Point René Ravaud-Réau, 77550 Moissy-Cramayel, France

Keywords: Multi-fidelity, Non-Intrusive POD, Surrogate-Based Optimization.

Abstract. *This paper presents a methodology for building multi-fidelity surrogate models based on Non-Intrusive Proper Orthogonal Decomposition. The proposed strategy aims at fusing multiple fidelity levels of simulation to improve the quality of surrogate models exploited in automated optimization loops of industrial-scale problems. A proof of concept is then given on a mathematical toy example which illustrates the ability of the proposed method to significantly reduce the overall computation cost. A 3D industrial study of a 1.5 stage booster is then presented to address the scaling capability of the proposed methodology.*

1 INTRODUCTION

Despite huge advances in the high performance computing domain, the integration of high-fidelity computations, taking up to thousands of CPU hours, into automated optimization loops still stands as a stumbling block for engineers. The design process being intrinsically multi-scale, multi-fidelity and multi-disciplinary [1]; the earlier the different scales, fidelities and disciplines are all integrated in the process, the better the technical solution can be [2, 3].

In this context, multi-fidelity surrogate modeling proposes a promising way to reduce the computational cost of industrial optimization [4]. The "data-fusion", also referred to as corrective approach in scaling methods [4, Section 6.1], enables the improvement of surrogate models [5] at a given computational cost. The most documented multi-fidelity model is the "co-Kriging" proposed by Kennedy and O'Hagan [6]. This technique has been widely applied to Multidisciplinary Design Optimization (MDO) [2, 5–11] and allows the enhancement of sparse high-fidelity information with cheaper low-fidelity data as well as the gradient of the modeled function [12, 13].

In the meantime, "Reduced-Order Models" (ROM) such as Proper Orthogonal Decomposition technique (POD) [14] have become very popular and their ability to focus on physical phenomena with highest impact on the performances targeted by the designer [15, 16] fosters their integration into new optimization strategies such as the "Non-Intrusive POD" (NI-POD) [17].

The aim of this work is to propose a methodology leveraging multi-fidelity computations during the training phase of an improved NI-POD model. This strategy can be seen as a re-interpretation of the constrained POD concept [15, 18] dedicated to multi-fidelity surrogate modeling. The methodology efficiency will be compared to classical NI-POD models as well as scalar mono- and multi-fidelity coKriging models.

The paper is organized as follows. Section 2 will present the NI-POD concept and the proposed extension. In Section 3, a proof of concept will be given on an academic example. Section 4 introduces the industrial application to illustrate the scalability of the proposed methodology. Finally, conclusions and perspectives are drawn in Section 5.

2 NON-INTRUSIVE POD

2.1 Classical NI-POD

POD, also known as "Karhunen-Loève expansion", or Principal Component Analysis (PCA) was introduced in the context of turbulence by Lumley [19] and allows to approximate high-dimensional numerical solution's output space by low-dimensional representation. The NI-POD methodology consists in building the orthonormal basis which optimally spans training database simulation's space and interpolating its coordinates in the basis via data-fitting methods [17].

The POD basis is computed by "snapshots" method [20] based on a Singular Value Decomposition (SVD) of M centered snapshots of the physical solution corresponding to M distinct positions $\boldsymbol{\Theta}$ in a p-dimensional design space $\mathcal{D} \subset \mathbb{K}^p$.

Let's consider a solver giving the physical response of any configuration in the design space $\mathcal{D}$,

$$\begin{aligned} \bar{\mathbf{s}} \ : \ \mathcal{D} &\rightarrow \mathbb{R}^n \\ \boldsymbol{\theta} &\rightarrow \bar{\mathbf{s}}(\boldsymbol{\theta}). \end{aligned} \tag{2.1}$$

The centered data are obtained by substracting the mean response over the training database $\mathbf{s}(\boldsymbol{\theta}) = \bar{\mathbf{s}}(\boldsymbol{\theta}) - \dfrac{1}{M}\sum_{i=1}^{M} \bar{\mathbf{s}}^{(i)}$. Following the formulation introduced in [21], the POD procedure gives the best projector $\mathcal{P}(\mathbf{s})$ on the orthonormal basis $\boldsymbol{\Phi}$ contained in the set of snapshots $\mathbf{S}$, in the sense of the Frobenius norm $\|A\|_F^2 = tr(A^\top A)$,

$$\boldsymbol{\Phi} = \underset{\boldsymbol{\Phi}}{argmin} \left(\|\mathbf{S} - \mathcal{P}(\mathbf{S})\|_F^2 \right), \text{ with } \boldsymbol{\Phi}^\top \boldsymbol{\Phi} = \mathbf{I}, \tag{2.2}$$

and,

$$\mathcal{P}(\mathbf{s}) = \boldsymbol{\Phi}\boldsymbol{\Phi}^\top \mathbf{s}. \tag{2.3}$$

The POD basis $\boldsymbol{\Phi}$ lies in a $\mathbb{R}^{M\times n}$ space where $M \ll n$. This ROM procedure is usually associated with a truncating step that removes the less energetic modes yielding a POD basis $\boldsymbol{\Phi}^m$ in $\mathbb{R}^{m\times n}$, where $m < M$ and characterized by the error $\epsilon(m) = 1 - \dfrac{\sum_{i=1}^{m} \boldsymbol{\lambda}_i}{\sum_{j=1}^{M} \boldsymbol{\lambda}_j}$, where $\boldsymbol{\lambda}$ is the vector of monotically decreasing eigenvalues associated with the basis $\boldsymbol{\Phi}$. In the coming sections, we consider a full basis of size M, for the sake of simplicity.

Denoting $\boldsymbol{\alpha} = \boldsymbol{\Phi}^\top \mathbf{s}(\boldsymbol{\theta})$ the coordinate of a given configuration $\boldsymbol{\theta}$ in the POD basis, the NI-POD procedure approximates the vector $\boldsymbol{\alpha} \in \mathbb{R}^M$ over the whole design space $\mathcal{D}$. Assuming a good predictive behaviour of the built surrogate model, the NI-POD procedure enables the engineer for predicting the full vectorial response at any location in $\mathcal{D}$.

$$\tilde{\mathbf{s}}(\boldsymbol{\theta}) = \boldsymbol{\Phi}\tilde{\boldsymbol{\alpha}}(\boldsymbol{\theta}), \tag{2.4}$$

where $\forall i \in [\![1, M]\!]$, $\tilde{\boldsymbol{\alpha}}_i = \widetilde{\alpha_i}(\boldsymbol{\theta}) \backsimeq \alpha_i(\boldsymbol{\theta})$. It is important to keep in mind that the type of the surrogate model chosen to approximate the coefficients is critical. Depending on the sampling method, the variations in the simulation output vector over the design space and on the number of training samples, different techniques could lead to either good or bad approximation. One can find a non-exhaustive list of potential models in Forrester et al. [5, Section I.2].

2.2 Proposed multi-fidelity extension to NI-POD based surrogate modeling:

Given the computational cost of industrial simulations, the number of known locations in the design spaces is usually relatively low reducing the representativeness of the POD basis $\boldsymbol{\Phi}$ over the whole design space $\mathcal{D}$. The integration of multi-fidelity information tends to address this limitation by improving the basis and the interpolation of the coefficients surrogate models thanks to cheaper low-fidelity solutions the engineer can compute more intensively. Adapting the constrained POD modeling method introduced by Xiao et al. [15, 18], we propose to append the POD basis with low-fidelity modes projected on the complementary space spanned

by the high-fidelity data available. In the meantime, we improve the predictive capabilities of the coefficients surrogate models by increasing the number of constraints they are submitted to. Indeed, while the sparse high-fidelity projection coefficients are interpolated by the surrogate models, the higher density of known low-fidelity projection coefficients gives information about the global trend the surrogate models should follow.

Let's consider an approximated solution associated with the simulation output of a complex system characterized by its position in a p-dimensional design space $\mathcal{D}$. Assuming the two levels of fidelity at hand are lying in spaces with matching dimensions, we can denote the low- and high-fidelity solutions respectively $\mathbf{s}_L$ and $\mathbf{s}_H$ both in $\mathbf{R}^n$,

$$\begin{aligned} \mathbf{s} \ &: \mathcal{D} \rightarrow \mathbf{R}^n \\ &\boldsymbol{\theta} \rightarrow \mathbf{s}_L(\boldsymbol{\theta}) \\ &\boldsymbol{\theta} \rightarrow \mathbf{s}_H(\boldsymbol{\theta}). \end{aligned} \tag{2.5}$$

We compute the low- and high-fidelity databases $\mathbf{S}_L$ and $\mathbf{S}_H$ assuming the solutions $\mathbf{s}$ are already centered as presented in Section 2.1 on two Design of Experiments (DoE) $\boldsymbol{\Theta}_L$ and $\boldsymbol{\Theta}_H$.

$$\begin{aligned} \mathbf{S}_L(\boldsymbol{\Theta}_L) &= \begin{bmatrix} s_1^L(\boldsymbol{\theta}^{(1)}) & & s_1^L(\boldsymbol{\theta}^{(M_L)}) \\ \vdots & \cdots & \vdots \\ s_n^L(\boldsymbol{\theta}^{(1)}) & & s_n^L(\boldsymbol{\theta}^{(M_L)}) \end{bmatrix} \quad , \ \forall \boldsymbol{\theta}^{(i)} \in \boldsymbol{\Theta}_L \\ \mathbf{S}_H(\boldsymbol{\Theta}_H) &= \begin{bmatrix} s_1^H(\boldsymbol{\theta}^{(1)}) & & s_1^H(\boldsymbol{\theta}^{(M_H)}) \\ \vdots & \cdots & \vdots \\ s_n^H(\boldsymbol{\theta}^{(1)}) & & s_n^H(\boldsymbol{\theta}^{(M_H)}) \end{bmatrix} \quad , \ \forall \boldsymbol{\theta}^{(i)} \in \boldsymbol{\Theta}_H \end{aligned} \tag{2.6}$$

Usually, the number of low-fidelity experiments will be higher $M_L > M_H$, and no nested sampling is here required to build the DoE's $\boldsymbol{\Theta}_L$ and $\boldsymbol{\Theta}_H$. One should notice that all the presented notions are straightforwardly extendable to more than 2 different levels of fidelity.

2.2.1 Multi-fidelity basis

We first seek the best definition of the space spanned by the high-fidelity simulation output via a QR decomposition,

$$\mathbf{S}_H = [\mathbf{Q}_1 \ \mathbf{Q}_2] \, [\mathbf{R}_1 \ \mathbf{0}]^\top. \tag{2.7}$$

$\mathbf{Q}_1$ is an orthonormal basis spanning the high-fidelity image of the high-fidelity DoE while $\mathbf{Q}_2$ is a non-unique description of the complementary space of the space spanned by the basis $\mathbf{Q}_1$.

As the two simulation output spaces are both lying in $\mathbf{R}^n$, we can project the low-fidelity database $\mathbf{S}_L$ onto $\mathbf{Q}_2$ and perform an SVD to find the best projector for the low-fidelity information in the complementary space of the high-fidelity information

$$\mathbf{V} \boldsymbol{\lambda} \mathbf{U}^\top = \mathbf{Q}_2^\top \mathbf{S}_H \ . \tag{2.8}$$

We define the multi-fidelity POD basis $\mathbf{\Psi}$ in Eq. 2.9 as the best projector for the low-fidelity information with a cancelling constraint on the high-fidelity error

$$\mathbf{\Psi} = [\mathbf{Q}_1 \;\; \mathbf{Q}_2\mathbf{V}]\,, \tag{2.9}$$

with $\mathbf{\Psi} \in \mathbb{R}^{(M_L+M_H)\times n}$.

2.2.2 Multi-fidelity coefficients surrogate model

Once the multi-fidelity POD basis $\mathbf{\Psi}$ is created, the final steps of the classical NI-POD procedure 2.1 are repeated. Given two databases, the information used for building the surrogate model is tagged by its level of fidelity. We first project the low- and high-fidelity databases $\mathbf{S}_L$ and $\mathbf{S}_H$ on the basis $\mathbf{\Psi}$. This step enables the construction of data-fitting models on every real-valued coordinate of the vectors of coefficients $\boldsymbol{\alpha}$.

The surrogate modeling techniques dealing with multi-fidelity databases are of two kinds. The category of nested sampling based models does not restrain the high-fidelity database to any subset of the low-fidelity database. This category being the less used in the literature, we will focus on multi-fidelity surrogate models based on nested DoE's such as classical corrective models. We first project the two nested databases $\mathbf{S}_L$ and $\mathbf{S}_H$ onto $\mathbf{\Psi}$ and use the low-fidelity coefficients of projection to create a low-fidelity Radial Basis Function Network (RBFN) model $\tilde{\boldsymbol{\alpha}}_L(\boldsymbol{\theta}),\ \forall \boldsymbol{\theta} \in \mathcal{D}$. Then we build another RBFN model of the difference between low- and high-fidelity coefficients and define the coefficients approximation as the sum of the two previous models. The proposed model is an additive scaling model defined in Eq. 2.10 where the models $\tilde{\boldsymbol{\delta}}_{H-L}(\boldsymbol{\theta})$ and $\tilde{\boldsymbol{\alpha}}_L(\boldsymbol{\theta})$ are one hidden-layer artificial neural networks

$$\tilde{\boldsymbol{\alpha}}_H(\boldsymbol{\theta}) = \tilde{\boldsymbol{\delta}}_{H-L}(\boldsymbol{\theta}) + \tilde{\boldsymbol{\alpha}}_L(\boldsymbol{\theta}) \;\; \forall \boldsymbol{\theta} \in \mathcal{D}\,. \tag{2.10}$$

3 VALIDATION ON MATHEMATICAL FUNCTIONS

In this section, the developed multi-fidelity NI-POD model is used to approximate vectorial analytical functions with different training sets. Various mathematical functions are referenced in the literature for the validation of optimization methodologies, but none, to the authors knowledge, exhibits a referenced low-fidelity definition and a multi-dimensional output space. We decided to derive our analytical test case from the multi-fidelity examples in [7] and [22, Section 3.5] as detailed in the coming section.

3.1 Mathematical definition

We assume two solvers associated with the functional solutions in Eq. 3.2. A 2-dimensional "design" space $\mathcal{D}$ is created by parameterizing the low- and high-fidelity solutions defining a 1-dimensional function

$$\begin{aligned} f : \mathcal{D} &\to \mathcal{F} \subset \mathcal{C}^\infty[0,1] \\ \boldsymbol{\theta} &\to f_{l_{\boldsymbol{\theta}}}(x) \\ \boldsymbol{\theta} &\to f_{h_{\boldsymbol{\theta}}}(x) \end{aligned} \tag{3.1}$$

with

$$
\begin{aligned}
f_{l_{\boldsymbol{\theta}}}(x) &= 0.5\left((\theta_1 x - 2)^2 \cdot \sin(12x - 4)\right) + \theta_2(x - 0.5) + 5, \\
f_{h_{\boldsymbol{\theta}}}(x) &= 0.5(\theta_1 x - 2)^2 \cdot \sin(12x - 4) + \sin(\theta_2 \cos(5x)).
\end{aligned}
\tag{3.2}
$$

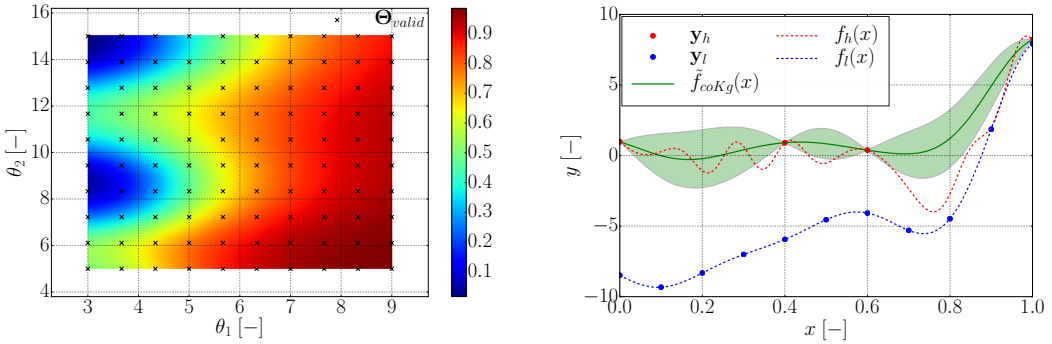

(a) Evolution of the Pearson's correlation coefficient over $\mathcal{D}$ (with bi-cubic interpolation)

(b) Low- and high-fidelity functions at reference location ($\theta_1 = 6$, $\theta_2 = 10$)

Figure 3.1: Correlation between low- and high-fidelity functions

Two vectorial solutions $\mathbf{s}_L$ and $\mathbf{s}_H$ are extracted from the functions $f_{l_{\boldsymbol{\theta}}}(x)$ and $f_{h_{\boldsymbol{\theta}}}(x)$ by sampling the $[0, 1]$-interval with 100 points evenly spaced. A first 10-level full factorial DoE $\boldsymbol{\Theta}_{valid}$ can show the correlation between low- and high-fidelity levels represented by its Pearson's correlation coefficient [23] painted on Figure 3.1a. We can distinguish different regions in the design space, some with good agreement (Fig. 3.2b) between low- and high-fidelity solutions and others where low- and high-fidelity are completely decorrelated (Fig. 3.2a), while the reference point (Fig. 3.1b) inspired by [7] and [22, Section 3.5] presents an average correlation level. As illustrated on Figure 3.2, the $2 - \sigma$ area (green shaded) of the coKriging model $\tilde{f}_{coKg}(x)$ is highly dependent on the low- to high-fidelity correlation intensity.

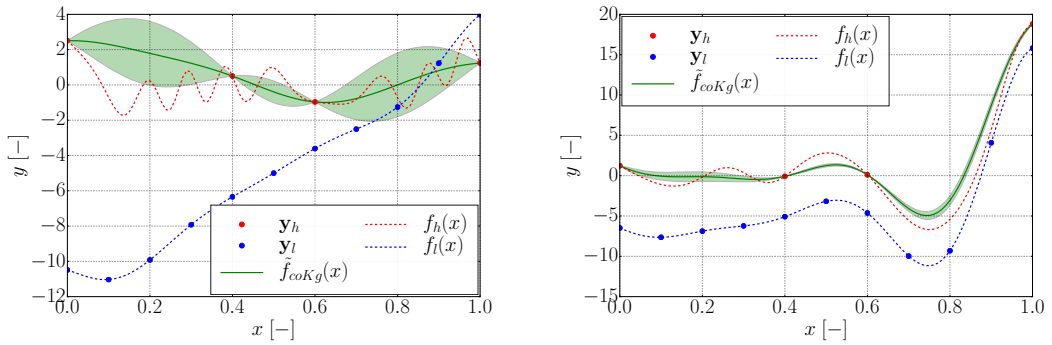

(a) Uncorrelated low- and high-fidelity functions ($\theta_1 = 4$, $\theta_2 = 14$)

(b) Strongly correlated low- and high-fidelity functions ($\theta_1 = 8$, $\theta_2 = 6$)

Figure 3.2: Range of correlations between low- and high-fidelity functions

3.2 Design of Experiments

Multiple nested Latin Hypercube DoE's ($\boldsymbol{\Theta}_H \subset \boldsymbol{\Theta}_L$) are created to assess the predictive performance of the proposed multi-fidelity model. Figure 3.3 shows a possible repartition of training points for a $2 + 10$ samples multi-fidelity DoE in the design space. The next section will present the results obtained with the proposed methodology in comparison with classical NI-POD models.
As the definition of a Latin Hypercube Sampling (LHS) is not unique, a statistical analysis of the impact of the training set on the model performances will be given for models trained on 100 different LHS for each couple (M_L, M_H).

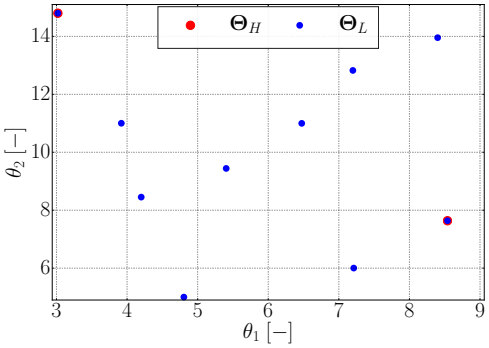

Figure 3.3: Multi-fidelity DoE in the design space $\mathcal{D}$ with $(M_L, M_H) = (10, 2)$

3.3 Results and classical NI-POD comparison

The performances of the proposed approach have to be evaluated in two phases. First, we want to assess the impact of the low-fidelity information gathered all over the design space on the quality of the multi-fidelity POD basis $\boldsymbol{\Psi}$ with respect to two representative bases:

- $\boldsymbol{\Phi}$: POD basis trained from $\mathbf{S}_H(\boldsymbol{\Theta}_H)$
- $\boldsymbol{\Phi}_\forall$: POD basis trained from $\mathbf{S}_H(\boldsymbol{\Theta}_L)$

The POD basis $\boldsymbol{\Phi}$ can be seen as the computational cost equivalent basis assuming the low-fidelity solution is almost free whereas the POD basis $\boldsymbol{\Phi}_\forall$ is the "best" basis we would have if we could afford intensive use of the high-fidelity solver.

3.3.1 Comparison of POD basis quality

Considering the DoE illustrated on Figure 3.3, the three basis $\boldsymbol{\Psi}$, $\boldsymbol{\Phi}$, and $\boldsymbol{\Phi}_\forall$ are built and the absolute L_2-error of the POD reconstruction of the solution $\mathbf{S}_H(\boldsymbol{\Theta}_{valid})$ is shown on Figure 3.4. The represented errors are expressed as following for any sample point in the design space $\mathcal{D}$ computed with the high-fidelity solver:

- $\epsilon_{\boldsymbol{\Phi}}(\boldsymbol{\theta}) = \sqrt{\frac{\|\mathbf{s}_H(\boldsymbol{\theta}) - \boldsymbol{\Phi}\boldsymbol{\Phi}^\top \mathbf{s}_H(\boldsymbol{\theta})\|^2}{\|\mathbf{s}_H(\boldsymbol{\theta})\|^2}}$
- $\epsilon_{\boldsymbol{\Phi}_\forall}(\boldsymbol{\theta}) = \sqrt{\frac{\|\mathbf{s}_H(\boldsymbol{\theta}) - \boldsymbol{\Phi}_\forall\boldsymbol{\Phi}_\forall^\top \mathbf{s}_H(\boldsymbol{\theta})\|^2}{\|\mathbf{s}_H(\boldsymbol{\theta})\|^2}}$
- $\epsilon_{\boldsymbol{\Psi}}(\boldsymbol{\theta}) = \sqrt{\frac{\|\mathbf{s}_H(\boldsymbol{\theta}) - \boldsymbol{\Psi}\boldsymbol{\Psi}^\top \mathbf{s}_H(\boldsymbol{\theta})\|^2}{\|\mathbf{s}_H(\boldsymbol{\theta})\|^2}}$

One can notice that the information introduced into the multi-fidelity basis construction process globally reduces the absolute L_2-error in the design space (Fig. 3.4c). This is due to the enrichment of the basis with orthogonal modes taken from the low-fidelity solutions supposed to be relatively close to the high-fidelity solution. Adding these modes in the complementary of the high-fidelity output space cancels any contamination of the basis by incoherent information from the low-fidelity solutions. We can also see (Fig. 3.4b) that for this 2-dimensional design space, 10 samples are sufficient to drop drastically the reconstruction error.

The proposed multi-fidelity POD basis tends to reduce the reconstruction error in both badly and strongly correlated low- and high-fidelity levels areas. This reduction of reconstruction error has to be confirmed after the surrogate modeling of the POD coefficients step.

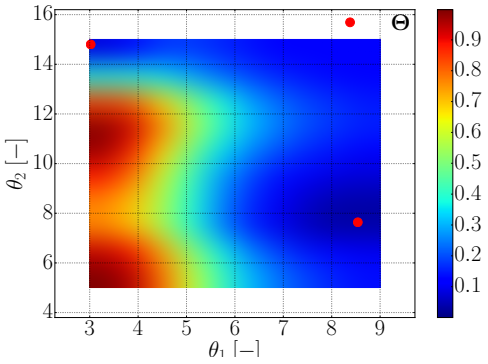

(a) L_2-error of the $\mathbf{\Phi}$-projector : $\epsilon_{\mathbf{\Phi}}(\boldsymbol{\theta})$

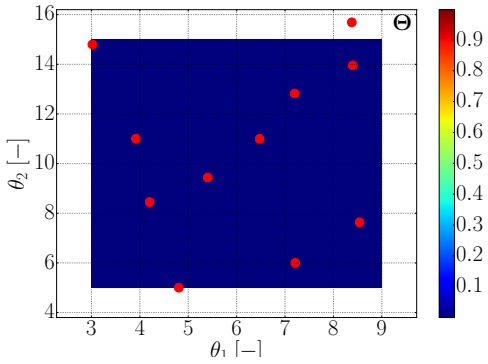

(b) L_2-error of the $\mathbf{\Phi}_\forall$-projector : $\epsilon_{\mathbf{\Phi}_\forall}(\boldsymbol{\theta})$

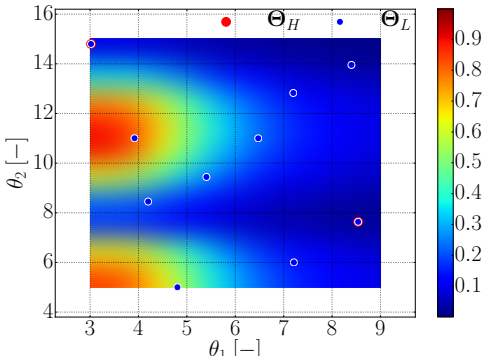

(c) L_2-error of the $\mathbf{\Psi}$-projector : $\epsilon_{\mathbf{\Psi}}(\boldsymbol{\theta})$

Figure 3.4: Absolute L_2-error of the POD reconstruction over $\mathcal{D}$

3.3.2 Comparison of NI-POD models quality

Once the POD basis is built, the training points are projected onto the basis and surrogate models are created to fit the coefficients databases. The chosen surrogate models are RBFN with tuned kernel and widths. For the proposed methodology, the surrogate model described on Equation 2.10 is used for each dimension of the vector of coefficients $\boldsymbol{\alpha}$.

Figure 3.5 presents the prediction error, hereafter detailed, of the three NI-POD models compared:

- $\mathbf{\Phi}\tilde{\boldsymbol{\alpha}}(\boldsymbol{\theta})$: NI-POD model trained on $\mathbf{S}_H(\mathbf{\Theta}_H)$,
  with scalar mono-fidelity RBFN for $\tilde{\alpha}_i \; \forall i \in [\![1, M_H]\!]$
- $\mathbf{\Phi}_\forall\tilde{\boldsymbol{\alpha}}_\forall(\boldsymbol{\theta})$: NI-POD model trained on $\mathbf{S}_H(\mathbf{\Theta}_L)$,
  with scalar mono-fidelity RBFN for $\tilde{\alpha}_i \; \forall i \in [\![1, M_L]\!]$
- $\mathbf{\Psi}\tilde{\boldsymbol{\alpha}}^+_{H,L}(\boldsymbol{\theta})$: NI-POD model trained on $\mathbf{S}_H(\mathbf{\Theta}_H) \cup \mathbf{S}_L(\mathbf{\Theta}_L)$,
  with scalar multi-fidelity RBFN (Eq. 2.10) for $\tilde{\alpha}_i \; \forall i \in [\![1, M_H + M_L]\!]$.

We can see on Figure 3.5b that for this test case, the 10 samples are sufficient to build a very good approximation of the POD coefficients as well. The maximum error observed in the lower-left corner of the design space on Figure 3.5a appears reduced on the Figure 3.5c as low-fidelity information is added to the model in regions where the low- to high-fidelity correlation coefficient is higher than 0.4 (Fig. 3.1a).

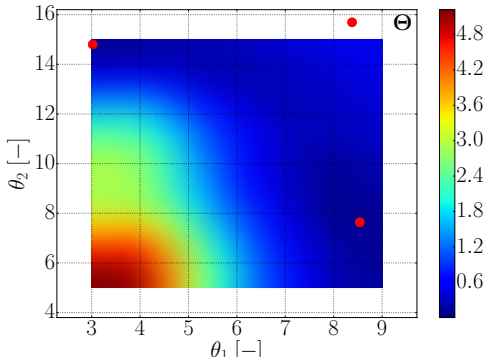

(a) L_2-error of the $\mathbf{\Phi}\tilde{\boldsymbol{\alpha}}$-predictor : $\epsilon_{\mathbf{\Phi}\tilde{\boldsymbol{\alpha}}}(\boldsymbol{\theta})$

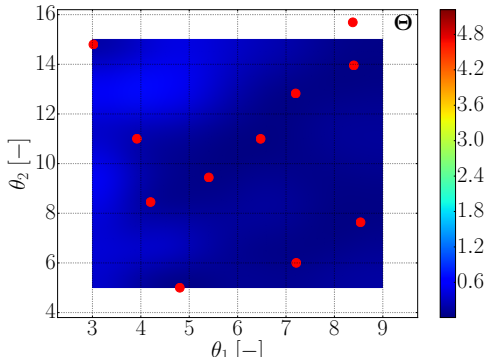

(b) L_2-error of the $\mathbf{\Phi}_\forall\tilde{\boldsymbol{\alpha}}_\forall$-predictor : $\epsilon_{\mathbf{\Phi}_\forall\tilde{\boldsymbol{\alpha}}_\forall}(\boldsymbol{\theta})$

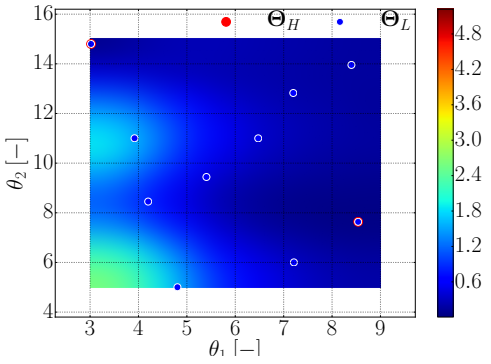

(c) L_2-error of the $\mathbf{\Psi}\tilde{\boldsymbol{\alpha}}^+_{H,L}$-predictor : $\epsilon_{\mathbf{\Psi}\tilde{\boldsymbol{\alpha}}^+_{H,L}}(\boldsymbol{\theta})$

Figure 3.5: Absolute L_2-error of the NI-POD prediction over $\mathcal{D}$

It is also important to keep in mind that the projection of the low-fidelity information on the complementary of the high-fidelity output space tends to reduce the impact of the POD coefficients associated with low-fidelity related modes as their contribution at high-fidelity location is cancelled. This behaviour is responsible for the non-pollution of the multi-fidelity NI-POD model in the top-left corner where both low- and high-fidelity are available and bad correlation coefficient is observed on Figure 3.1a.

3.3.3 Statistical analysis

To validate the impact of the proposed methodology in terms of computational cost, we propose to estimate the mean absolute L_2-error $\bar{\epsilon}$ over the entire design space depending on the size of the DoE's $\boldsymbol{\Theta}_H$ and $\boldsymbol{\Theta}_L$ and on the NI-POD based surrogate modeling technique. The construction of any DoE given couple of sizes (M_H, M_L) being non-unique, we build 100 independent DoE's for every couple $(M_H, M_L) \in [\![2]\!] \times [\![2, 28]\!]$. Figure 3.6 shows the decreasing trend of $\bar{\epsilon}_{\boldsymbol{\Phi}_\forall \tilde{\boldsymbol{\alpha}}_\forall}$ while $\bar{\epsilon}_{\boldsymbol{\Phi}\tilde{\boldsymbol{\alpha}}}$ remains statistically stable meaning that the 100-DoE's samples are sufficient to determine coherent conclusions for the study case at hand. We can also observe that the mean error associated with the proposed surrogate model $\bar{\epsilon}_{\boldsymbol{\Psi}\tilde{\alpha}^+_{h,l}}$ starts decreasing with added low-fidelity training points before stabilizing after $M_L > 8$. Once all the high-fidelity information lying in low-fidelity solutions is added to the POD basis, the computation of new low-fidelity experiments becomes useless and new high-fidelity computations are required to reduce further the global error of the surrogate model.

Statistical errors have also been compared for higher number of high-fidelity training snapshots and led to the same conclusions. These results are not illustrated because of too fast drop in the mean error due to the fact that the design space $\mathcal{D}$ is low-dimensional in this case ($p = 2$).

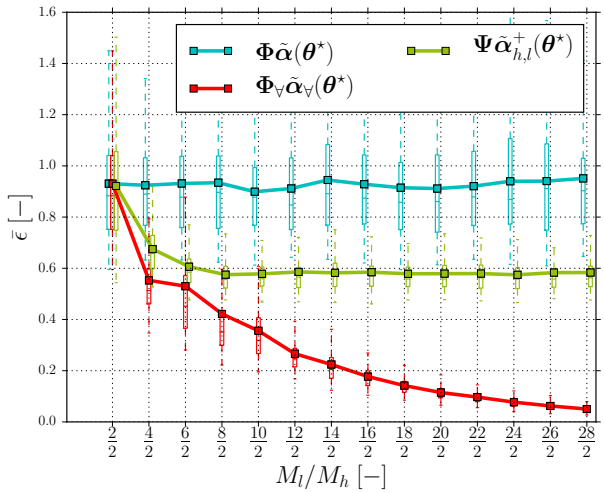

Figure 3.6: Evolution of the mean error $\bar{\epsilon}$ over $\mathcal{D}$ depending on the modeling technique

To investigate further the performance of the proposed modeling technique, we intend to test its efficiency on an industrial application presented hereafter.

4 INDUSTRIAL APPLICATION AND RESULTS

Aerodynamic design of Low-Pressure Compressors (LPC) is of major interest for jet engine manufacturers. The economical, technical and environmental constraints applied to turbofan designs force engineers to make a tradeoff between stage loading and both component efficiency and stability. Based on previous work presented by Lepot et al. [24], we propose to improve classical NI-POD surrogate models by adding low-fidelity information from coarse mesh based simulations.

4.1 Test case presentation

The test case presented in [24] consists in a surrogate-assisted optimization of a 1.5 stage booster based on $3D$ RANS simulations. The computational domain contains the inlet vane, the first rotating row and its following stator as illustrated on Figure 4.1. The deformed geometries are restrained to the rotating row, where the blade stacking as well as the hub axisymmetric profiling are parameterized respectively by 2 and 17 parameters. The geometric deformations are performed by either an in-house blade shape modeler for the stacking modifications or *CATIA v5R21* for the hub profiling. 3-level multigrid meshes are generated by *Autogrid v9r1.1* and $3D$ RANS simulations are computed by *elsA v3.3p1* [25]. Both high- and low-fidelity computations are conducted with $k-\varepsilon$ turbulence model without any near-wall treatment.

High-fidelity simulations are based on a structured mesh of about 5 million points preserving a y+ value below 1 along blades and endwalls. The convergence is accelerated thanks to a 2-level multigrid V-cycling leading to an overall run time around 2 hours for both design and near stall configurations on 32 Intel Xeon E5-2680v3 computation cores of Cenaero's cluster. Low-fidelity computations are performed on the mesh χ_{lf}, obtained by isotropic coarsening of the high-fidelity mesh χ_{hf}, leading to execution time around 15 minutes.

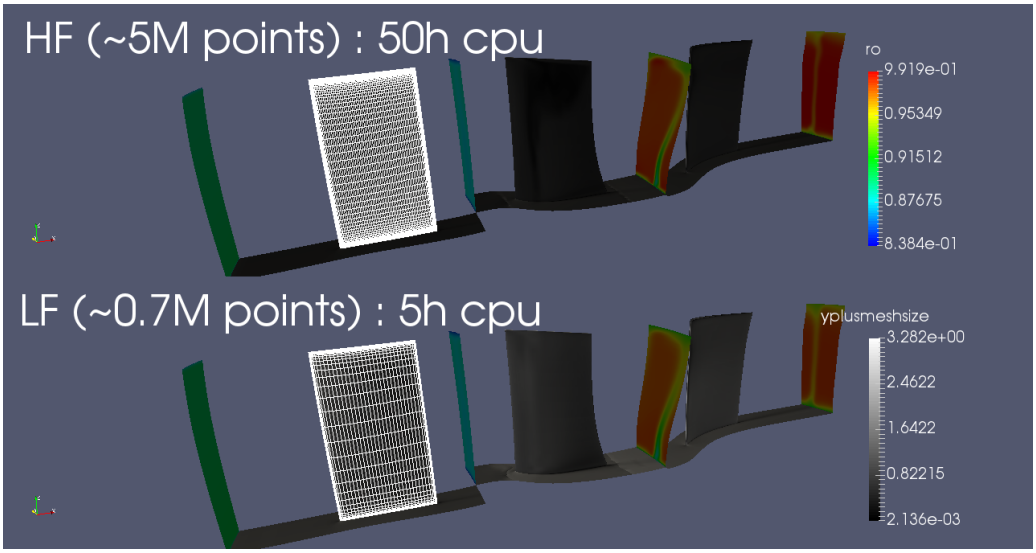

Figure 4.1: Low- and high-fidelity computational domains with isocontour of surface mesh coefficient y^+ and ρ distribution on mixing planes

4.2 Snapshot definition

We chose to approximate the conservative variables of the $3D$ computation in 4 sections defined by the inlet, outlet and inter-rows mixing planes. The definition of every mixing plane is

orthogonal to the revolution axis of the engine which avoid important mesh interpolation efforts.

As explained in Section 2.2, the low- and high-fidelity solutions lie in spaces with matching dimensions. The high-fidelity solution is therefore considered only at low-fidelity mesh point locations ("coarsening" step) to train the multi-fidelity NI-POD model and to compute scalar indicators such as isentropic efficiency. Figure 4.2 shows the impact of "coarsening" the high-fidelity solution on the computation of isentropic efficiency at design point η. We can see that considering high-fidelity solution only on the low-fidelity mesh χ_{lf} has a negligible impact on the isentropic efficiency. Indeed, the efficiency computed from the "coarsened" high-fidelity solution $\eta_{hf}[\chi_{lf}]$ (green points) is very close to the one integrated from the computed high-fidelity solution η_{hf} (red line). On the contrary, the isentropic efficiency integrated from low-fidelity solutions η_{lf} (blue points) presents non-negligible error with respect to the perfect match line (red line).

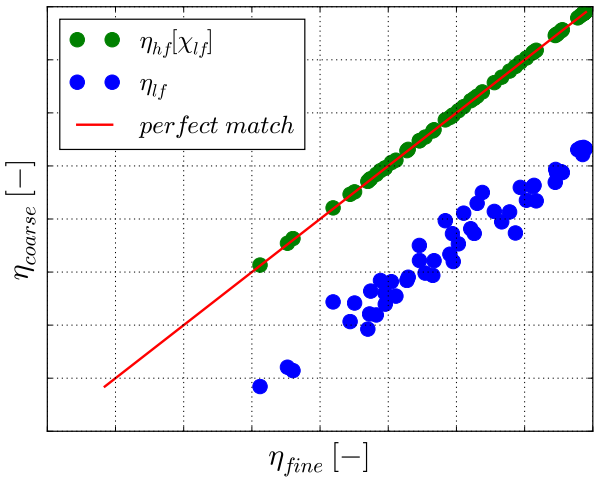

Figure 4.2: Low- to high-fidelity correlation of the efficiency for the 1.5 stage compressor at design configuration

4.3 Design of Experiments and multi-fidelity NI-POD

Given the overall computational cost of high-fidelity solutions, we decided to perform a 100-points DoE to train the proposed multi-fidelity NI-POD models as well as the POD and data-fitting based models used for validation purposes. Both the low- and high-fidelity solutions of the 100 training points are computed enabling a pseudo-statistical study of the impact of high-fidelity training samples on models performances. The success rate of the overall computation chain is about 60% removing all *CATIA* regeneration failures and all meshes with minimal skewness angle lower than 3°.

The presented results only concern the design point performance approximations. By randomly selecting high-fidelity solutions for a part of the training DoE we seek the impact of a priori sampling on the surrogate model quality. Different models are compared at predicting the high-fidelity design point efficiency computed for a 200-points validation DoE:

- Reconstruction capabilities assessment :

1. POD model built on the high-fidelity training set only $\mathbf{\Phi}\mathbf{\Phi}^\top$s
2. POD model built on a high-fidelity training set computationally equivalent to the multi-fidelity database $\mathbf{\Phi}_{ce}\mathbf{\Phi}_{ce}^\top$s
3. multi-fidelity POD model built on the high-fidelity training set enhanced by all low-fidelity training solutions $\mathbf{\Psi}\mathbf{\Psi}^\top$s

- Prediction capabilities assessment :

1. NI-POD model built on the high-fidelity training set only $\mathbf{\Phi}\tilde{\boldsymbol{\alpha}}$
2. NI-POD model built on a high-fidelity training set computationally equivalent to the multi-fidelity database $\mathbf{\Phi}_{ce}\widetilde{\boldsymbol{\alpha}_{ce}}$
3. multi-fidelity NI-POD model built on the high-fidelity training set enhanced by all low-fidelity training solutions $\mathbf{\Psi}\tilde{\boldsymbol{\alpha}}^+$
4. mono-fidelity tuned radial basis function network built on the high-fidelity training set $\tilde{\eta}$
5. mono-fidelity tuned radial basis function network built on a high-fidelity training set computationally equivalent to the multi-fidelity database $\tilde{\eta}_{ce}$

4.4 Results

Figure 4.3 shows a comparison of the reconstruction capabilities of all POD-based models. One can see that the reconstruction error of all 3 models ($\mathbf{\Phi}\mathbf{\Phi}^\top$s, $\mathbf{\Phi}_{ce}\mathbf{\Phi}_{ce}^\top$s, and $\mathbf{\Psi}\mathbf{\Psi}^\top$s) is very low as the circles are close to the perfect match line (in red). This means that the POD basis contains already ($M_H \approx p$, where $\mathcal{D}$ is p-dimensional) all the modal information needed to reproduce the conservative variables distributions of the 110 successfully computed samples in the validation DoE. Note that the reconstruction capability of a POD based model is totally useless for a "real world" application as projecting a solution on the POD basis first requires the expensive computation it is derived from.

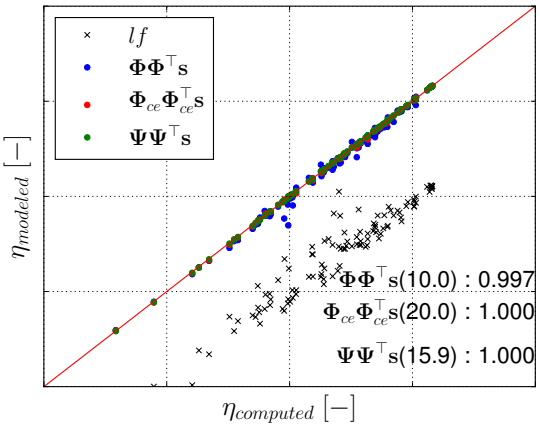

Figure 4.3: Computed- to modeled-efficiency correlation for POD-based models reconstruction

On the contrary, the predictive capabilities of NI-POD based models present more differences depending on the chosen approach (see Fig. 4.4a). The integration of low-fidelity points for

the training step increases the quality (correlation coefficients on Fig 4.4) of the proposed model with both respect to classical NI-POD models and mono-fidelity scalar RBF-based models (Fig. 4.4b). We can see on Fig. 4.4a that the green points (associated to the isentropic efficiency prediction of the proposed model) are closer on average to the perfect match line than the blue and red points (associated to the isentropic efficiency prediction of classical NI-POD models). The same observation can be made for mono-fidelity RBFN based models (see Fig. 4.4b).

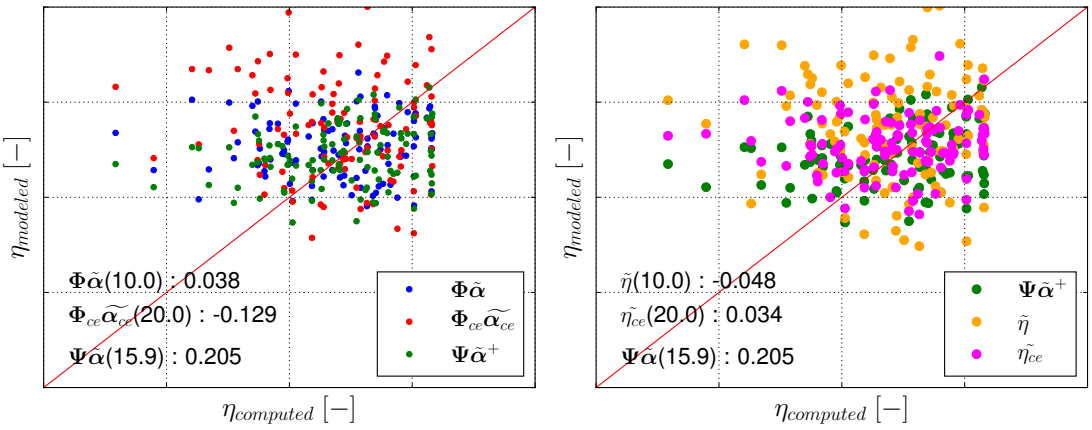

(a) Computed- to modeled-efficiency correlation for NI-POD based models prediction

(b) Computed- to modeled-efficiency correlation for radial basis function based models prediction

Figure 4.4: Comparison of predictive capabilities of NI-POD and radial basis functions based models

As mentioned earlier, we try to study the impact of the initial high-fidelity training set $\mathbf{\Theta}_H$ on the models quality. Table 1 shows that the proposed methodology is responsible on average for an increase of the model quality and tends to limit the impact of the initial DoE.

		Pearson's coefficient (μ)	Pearson's coefficient (σ)	CPU cost (μ)
POD	$\mathbf{\Phi\Phi}^\top\mathbf{s}$	0.9913	0.0311	10.7
	$\mathbf{\Phi}_{ce}\mathbf{\Phi}_{ce}^\top\mathbf{s}$	0.9996	0.0008	17.7
	$\mathbf{\Psi\Psi}^\top\mathbf{s}$	1.0000	0.0000	16.6
NIPOD	$\mathbf{\Phi}\tilde{\boldsymbol{\alpha}}$	0.0586	0.1611	10.7
	$\mathbf{\Phi}_{ce}\widetilde{\boldsymbol{\alpha}_{ce}}$	0.0803	0.1558	17.7
	$\mathbf{\Psi}\tilde{\boldsymbol{\alpha}}^+$	0.1816	0.0588	16.6
RBF	$\tilde{\eta}$	0.0707	0.1573	10.7
	$\tilde{\eta}_{ce}$	0.0763	0.1491	17.7

Table 1: Mean and standard deviation of Pearson's correlation coefficients for different models trained with 50 different $\mathbf{\Theta}_H$ of given mean costs

As the selection of high-fidelity training points is non-uniformly random, the overall cost of training points computation is not constant. The mean value of training CPU costs is given in

Table 1, and shows that despite its higher mean training cost, the "computationally equivalent" high-fidelity trained NI-POD model presents lower quality that the proposed multi-fidelity model. This is due to higher coverage of the design space with low-fidelity samples improving globally the model quality.

5 CONCLUSIONS AND PERSPECTIVES

One can consider non intrusive-POD models as better integrators of physics than classical data-fitting based models. In the context of surrogate-assisted optimization, this leads to better insight in the relation between design parameters and performance indicators and similarly between parameters and the global system behaviour. Based on this assumption, the current paper has presented an extension of non-intrusive POD to multi-fidelity design. The proposed methodology leverages relatively high density of low-fidelity solutions in the design space to enhance both the POD basis and the surrogate models of coefficients of classical NI-POD models. First implementation of the presented technique has been tested on an analytical test case inspired by coKriging related articles [7, 22] and an industrial test case of a 1.5-stage low-pressure compressor [24].

The proposed model efficiency has been compared to classical NI-POD models and mono-fidelity RBFN-based models. The multi-fidelity NI-POD model significantly improved both the POD basis representativeness and the NI-POD predictive capabilities on the analytical test case. The results showed the contribution of low-fidelity samples in the prediction error of the model. At the same time, the potential limit in error reduction due to the lack of correlation between low- and high-fidelity solutions in some regions of the design space has been revealed.

The prediction error reduction, obtained from added low-fidelity information, has also been verified on the industrial scale problem in Section 4. The models performances have been compared on the isentropic efficiency at design point showing again the impact of densely spaced low-fidelity information. Despite relatively low correlations observed, the results showed a real potential of the proposed method to reach the objective of starting an optimization with DoE samples as large as the problem dimensionality ($M_H \approx p$).

Some issues remain to be addressed concerning the building methodology itself as well as some questions remain opened on the industrial application presented. The question of truncation is one of the cornerstones of NI-POD based approximation and is totally opened when dealing with multi-fidelity POD models. The impact of truncation has to be questionned especially for problems where only a few modes are needed but highly non-linear behaviour is observed for projection coefficients. The impact of snapshot definition is also to be investigated. In the presented test case, the stacking deformation incited us to post-process conservative variables only on mixing planes. Because of relatively important distances between rows and diffusion, the physical complexity of wake and secondary flows can vanish and be missed in the integrated snapshots. The extension of the proposed study to other performance indicators and off-design configurations would allow more precise comparison with the results highlighted in [24].

In terms of general perspectives, a comparison with Kriging or coKriging models could be considered in future work where none is presented in this study because of the hyper-parameters optimization cost in high-dimensional design space. Last but not least, the integration of the proposed methodology in an automated optimization loop has also to be performed and would

check the validity of the given observations for higher correlation coefficients needed for a successfull surrogate-assisted optimization.

Acknowledgements

The present work was partly founded by the *Association Nationale de la Recherche et Technologie*. The authors would like to thank *Snecma* and *Techspace Aero* from the *SAFRAN Group* for their support and permission to publish this study and especially Ir. Stephane Hiernaux and Ir. Jean Coussirou for their technical support in this research project.

References

[1] E. Tromme, O. Brüls, J. Emonds-Alt, M. Bruyneel, G. Virlez, and P. Duysinx. "Discussion on the optimization problem formulation of flexible components in multibody systems". In: *Structural and Multidisciplinary Optimization* 48.6 (2013), pp. 1189–1206.

[2] A. March and K. Willcox. "Constrained multifidelity optimization using model calibration". In: *Structural and Multidisciplinary Optimization* 46.1 (May 2012), pp. 93–109.

[3] A. J. Keane. "Wing optimization using design of experiment, response surface, and data fusion methods". en. In: *Journal of Aircraft* 40 (July 2003), pp. 741–750.

[4] A. J. Keane and P. B. Nair. *Computational Approaches for Aerospace Design: The Prusuit of Excellence*. John Wiley & Sons, 2005.

[5] A. I. J. Forrester, A. Sóbester, and A. J. Keane. *Engineering Design via Surrogate Modelling : A Practical Guide*. John Wiley & Sons, 2008.

[6] M. C. Kennedy and A. O'Hagan. "Predicting the output from a complex computer code when fast approximations are available". In: *Biometrika* 87.1 (Jan. 2000), pp. 1–13.

[7] A. I. J. Forrester and A. J. Keane. "Recent advances in surrogate-based optimization". In: *Progress in Aerospace Sciences* 45.1-3 (Jan. 2009), pp. 50–79.

[8] Y. Kuya, K. Takeda, X. Zhang, and A. I. J. Forrester. "Multifidelity surrogate modeling of experimental and computational aerodynamic data sets". In: *AIAA Journal* 49.2 (Feb. 2011), pp. 289–298.

[9] D. J. Toal and A. J. Keane. "Efficient multipoint aerodynamic design optimization via cokriging". en. In: *Journal of Aircraft* 48.5 (Sept. 2011), pp. 1685–1695.

[10] L. Huang, Z. Gao, and D. Zhang. "Research on multi-fidelity aerodynamic optimization methods". en. In: *Chinese Journal of Aeronautics* 26.2 (Apr. 2013), pp. 279–286.

[11] Z.-H. Han, S. Görtz, and R. Hain. "A Variable-Fidelity Modeling Method for Aero-Loads Prediction". English. In: *New Results in Numerical and Experimental Fluid Mechanics VII*. Ed. by A. Dillmann, G. Heller, M. Klaas, H.-P. Kreplin, W. Nitsche, and W. Schröder. Vol. 112. Notes on Numerical Fluid Mechanics and Multidisciplinary Design. Springer Berlin Heidelberg, 2010, pp. 17–25.

[12] Z.-H. Han, R. Zimmermann, and S. Görtz. "A new cokriging method for variable-fidelity surrogate modeling of aerodynamic data". In: *Proc. 48th AIAA Aerospace Sciences Meeting Including the New Horizons Forum and Aerospace Exposition*. AIAA, Jan. 2010.

[13] Z.-H. Han, S. Görtz, and R. Zimmermann. "Improving variable-fidelity surrogate modeling via gradient-enhanced Kriging and a generalized hybrid bridge function". In: *Aerospace Science and Technology* 25.1 (Mar. 2013), pp. 177–189.

[14] P. Holmes, J. L. Lumley, G. Berkooz, and C. W. Rowley. *Turbulence, Coherent Structures, Dynamical Systems and Symmetry*. Second. Cambridge Books Online. Cambridge University Press, 2012.

[15] M. Xiao, P. Breitkopf, R. F. Coelho, P. Villon, and W. Zhang. "Proper orthogonal decomposition with high number of linear constraints for aerodynamical shape optimization". In: *Applied Mathematics and Computation* 247.0 (2014), pp. 1096–1112.

[16] R. Filomeno Coelho, P. Breitkopf, and C. Knopf-Lenoir. "Model reduction for multidisciplinary optimization - application to a 2D wing". In: *Structural and Multidisciplinary Optimization* 37.1 (2008), pp. 29–48.

[17] M. Guénot, I. Lepot, C. Sainvitu, J. Goblet, and R. Filomeno Coelho. "Adaptive sampling strategies for non-intrusive POD-based surrogates". In: *Engineering Computations* 30.4 (Jan. 2013), pp. 521–547.

[18] M. Xiao, P. Breitkopf, R. F. Coelho, C. Knopf-Lenoir, P. Villon, and W. Zhang. "Constrained Proper Orthogonal Decomposition based on QR-factorization for aerodynamical shape optimization". In: *Applied Mathematics and Computation* 223.0 (2013), pp. 254–263.

[19] J. L. Lumley. "The structure of inhomogeneous turbulent flows". In: *Atmospheric turbulence and radio propagation*. Ed. by A. M. Yaglom and V. I. Tatarski. Nauka, 1967, pp. 166–178.

[20] L. Sirovich. *Turbulence and the Dynamics of Coherent Structures, Part1: Coherent Structures*. Vol. 45. Quarterly of Applied Mathematics 3. Brown University, Division of Applied Mathematics, Oct. 1987, pp. 561–571.

[21] B. Raghavan, L. Xia, P. Breitkopf, and P. Villon. "Towards simultaneous reduction of both input and output spaces for interactive simulation-based structural design". In: *Computer Methods in Applied Mechanics and Engineering* 265 (July 2013), pp. 174–185.

[22] L. Le Gratiet. "Multi-fidelity Gaussian process regression for computer experiments". PhD thesis. Université Paris-Diderot-Paris VII, Oct. 2013, 306pp.

[23] K. Pearson. "Mathematical Contributions to the theory of evolution. III. Regression, Heredity, and Panmixia". In: *Philosophical Transactions of the Royal Society of London A: Mathematical, Physical and Engineering Sciences* 187 (1896), pp. 253–318.

[24] I. Lepot, T. Mengistu, S. Hiernaux, and O. De Vriendt. "Highly loaded LPC blade and non axisymmetric hub profiling optimization for enhanced efficiency and stability". In: *ASME Turbo Expo 2011: Turbine Technical Conference and Exposition*. Vol. 7. Jan. 2011, pp. 285–295.

[25] L. Cambier, S. Heib, and S. Plot. "The Onera elsA CFD software : input from research and feedback from industry". In: *Mechanics & Industry* 14.3 (Apr. 2013), pp. 159–174.